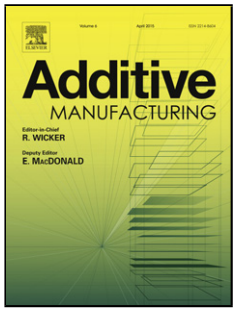

Title: Quality control of AlSi10Mg produced by SLM: metallography versus CT scans for critical defect size assessment

Authors: S. Romano, A. Abel, J. Gumpinger, A.D. Brandão, S. Beretta

PII: S2214-8604(19)30205-2
DOI: https://doi.org/10.1016/j.addma.2019.05.017
Reference: ADDMA 731

To appear in:

Received date: 19 February 2019
Revised date: 6 May 2019
Accepted date: 14 May 2019

Please cite this article as: Romano S, Abel A, Gumpinger J, Brandão AD, Beretta S, Quality control of AlSi10Mg produced by SLM: metallography versus CT scans for critical defect size assessment, *Additive Manufacturing* (2019), https://doi.org/10.1016/j.addma.2019.05.017

Quality control of AlSi10Mg produced by SLM: metallography versus CT scans for critical defect size assessment

S. Romano[a,*], A. Abel[b], J. Gumpinger[b], A.D. Brandão[b], S. Beretta[a]

[a]*Politecnico di Milano, Via La Masa 1, 20156, Milan, Italy*
[b]*ESA/ESTEC, European Space Research and Technology Center, Noordwijk, The Netherlands*

*Corresponding author
Email address: simone.romano@polimi.it (S. Romano)

Graphical abstract

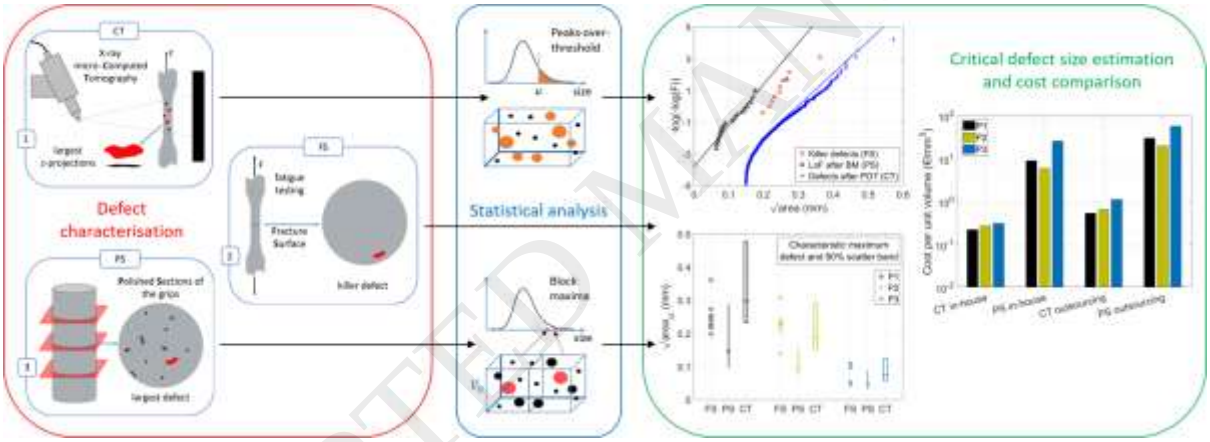

Highlights:

- The quality assessment of AM materials containing defects is a complex topic;
- Multiple defect types were characterised by X-ray CT and metallographic analysis;
- The critical defects in fatigue samples were compared to the statistical estimates;
- Quality correctly assessed by both methods for material obtained by three processes;
- Better precision and lower cost by CT when similar volumes are investigated.

Abstract

While the adoption of metal additive manufacturing (AM) is growing exponentially owing to its wide range of potential applications, its application to safety-critical and structural parts is significantly impeded by the lack of

standards. Quality assessment of AM products is a crucial requirement, as the AM process induces internal defects that can have detrimental effects on the fatigue resistance.

By evaluating the defect distribution, it is possible to perform a fracture mechanics assessment to estimate the fatigue strength and service lifetime of AM materials. This strategy has been successfully applied to selective laser-melted AlSi10Mg by performing X-ray micro-computed tomography (µCT) and applying suitable statistical methods (i.e., statistics of extremes). However, it remains unclear whether complex and expensive nondestructive inspection methods (e.g., µCT) are necessary and whether simpler and more conventional approaches (i.e., microscopy of polished sections (PSs), as prescribed by ASTM E2283) would provide equivalent information for the estimation of internal defects.

In this study, the size of the most detrimental defect was estimated by performing both light microscopy on PSs and µCT on three batches of fatigue specimens characterized by different internal porosities. The results showed that both techniques were able to pinpoint a significant difference in the prospective largest defect in a material volume corresponding to the gauge section of a specimen. However, extrapolation of the critical defect size for fatigue failure using PS data was less accurate and less conservative than that using CT data. An evaluation of the techniques with regard to time and cost indicated that µCT allowed the investigation of larger sample volumes and the reduction of both man hours and cost.

Keywords:

AlSi10Mg; material quality; defect; computed tomography; metallography

Nomenclature

Acronyms:

AM	additive manufacturing
BM	block maxima
(µ)CT	(micro-)computed tomography
FS	fracture surface
LEVD	largest extreme value distribution
LoF	lack of fusion
POT	peaks-over-threshold
PS	polished section
SEM	scanning electron microscopy
SIF	stress intensity factor
SLM	selective laser melting

Symbols:

F	cumulative distribution function
F_{exc}	cumulative distribution function of the exceedances over *u*
h_{mean}	average defect size recorded in S_0

K	SIF
n	number of extractions of a variable
N_u	number of exceedances over *u*
R_{sphere}	radius of the sphere equivalent to a defect in terms of volume
S	applied stress
S_{def}	defect surface
S_0	control area for 2D BM sampling
T	return period
u	threshold for POT maxima sampling
V	volume of material
V_c	prospective component volume
V_{def}	defect volume
V_{FS}	volume associated with FS analyses
V_{PS}	volume associated with PS analyses
V_{surf}	surface gauge volume of a fatigue sample
V_0	control volume for 3D BM sampling
x_p	*p*-percentile of a distribution
x_T	maximum characteristic value with a return period *T*
X, Z	variables
Z_n	maximum value over *n* extractions
σ	parameter of a negative exponential distribution function
λ, δ	parameters of an LEVD
ρ	density of the exceedances over *u*
$\sqrt{\mathrm{area}}$	Murakami's defect size parameter

1. Introduction

Additive manufacturing (AM) has been studied intensively in academia as well as in various industries for well over two decades. The very first laser powder bed-based machines were only able to fuse a low-melting point binder of a metallic, two-phase feedstock, but development quickly enabled the melting of pure, pre-alloyed powders. After industries discovered the potential of the emerging technology, the rate of development and applications steadily increased. Since then, the AM industry is undergoing exponential growth [1]. Almost every major stakeholder in the aerospace industry is assessing the disruptive potential of AM to enhance the performance of products [1–10].

Despite the vast application potential arising from the almost unlimited geometrical freedom, the current production speeds, i.e., the produced volume per unit time, are lower than those of traditional manufacturing techniques. Nevertheless, the space industry, which involves small production series and single-item fabrications, has been able to transform products through AM, resulting in sound business cases [4, 5, 7]. Many of the current flight applications are structures with low criticality, the designs of which are mostly driven by stiffness.

AM is increasingly used for highly critical applications, including primary, mission-critical structures and rocket propulsion elements [9–11]. Assessing the structural integrity of these parts is important, and requires strict control of the manufacturing process as well as testing of the produced material. The latter involves a variety of application-oriented mechanical tests, as well as tests of the physical properties, including the relative density.

Defects, which reduce the relative density, are typically pores, a lack of fusion (LoF), and irregularly shaped key-hole defects [12, 13]. These defects are typically associated with gaseous trace elements such as O [14] or H [15] or the energy input per volume unit (LoF and key-hole defects) [13]. In some cases, inclusions may also be present, although usually being less detrimental than pores and LoF [16]. Finally, clustering issues may randomly occur when the number of defect per unit volume is large [17,18], or in the sub-surface regions due to non-optimal process conditions [19,20].

Phenomenological approaches to examine the fatigue properties of AM materials have shown that fatigue life [21], as well as other mechanical properties [22], can be significantly affected by an increase in porosity. Therefore, the determination of the density has become a key element in assessing the quality of produced AM materials. For this, various techniques are currently applied or under investigation, including ultrasonic methods [23], the Archimedean method, microsectioning, and X-ray micro-computed tomography (µCT). While the first two methods only allow conclusions to be drawn regarding the relative density, microsectioning and X-ray µCT also provide insight into the nature and distribution of defects [21–25] (e.g., LoF, key-hole porosity, and inclusions).

The fatigue properties of AM materials are always associated with large scattering due to several factors, including heat treatment, surface finishing, and the microstructure (see the review concerning Ti-6Al-4V in [26]). Among the factors reported, a large part of the scattering observed in the fatigue properties is attributed to process-dependent defects [20]. The fatigue resistance in the absence of defects is comparable to or better than that for traditional manufacturing processes like casting or forging [25–27].

Defects can be analyzed in terms of stress raisers [28, 29] or by treating them as short cracks. From this viewpoint, a review conducted by Beretta and Romano showed that most of the scattering of the fatigue properties of Al alloys and Ti-6Al-4V obtained via AM is controlled by the variability of inhomogeneities at the origin of failures and that the sensitivity of the fatigue strength to the defect size is similar for AM and traditional processes [19]. One of the possible ways for estimating the fatigue strength is by considering the defects as short cracks and employing models (Murakami-Endo, Tanaka and Akiniwa, El-Haddad et al. [32]) that describe the relationship between the fatigue strength and the defect size (Kitagawa–Takahashi diagram [33]) or the dependence of the crack-propagation threshold on the crack size [33, 34]. This approach was examined in a study performed by Politecnico di Milano in collaboration with ESA and RUAG Space, in which an AlSi10Mg alloy produced via selective laser melting (SLM) according to three processes (P1–P3) with different porosity content was investigated [16]. The specifications of the processes are reported in Sec. 2. The results shown in Figure 1a indicate the different fatigue resistance among the processes and the large scattering. Measuring the size of the defects found at the origin of failure on the fracture surfaces (FSs) in terms of the root-area parameter [36] clearly reveals that the differences and scattering are mainly caused by the variability in the size of the killer defects, i.e., the defects at the origin of fatigue failures (see Figure 1b). For the three processes investigated, fractographic analyses highlighted that the root causes of fatigue crack initiation were LoF defects.

According to this defect-crack similarity, the fatigue life for the high-cycle fatigue and low-cycle fatigue regimes can be evaluated via fatigue crack growth simulations by adopting suitable formulations for the driving force at

the defect tip [35, 37, 38]. Similar conclusions regarding the effect of defects in AM materials and their analysis using the Kitagawa-Takahashi diagram were drawn in [39–41].

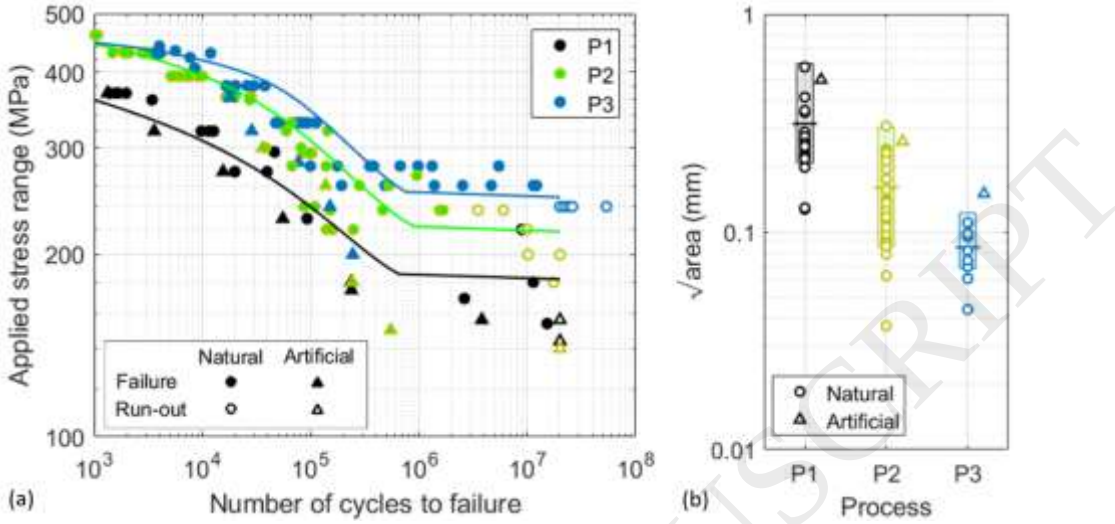

Figure 1: Results of the fatigue tests performed on three batches of material (R = -1) (adapted from [16]*): S-N curve and average estimates obtained by fracture mechanics approaches; (b) size of the critical defects and estimate based on µCT measurements (average plus 90% scatter band).*

One of the major consequences of the crack-defect similitude is that the fatigue strength of a given material volume is controlled by the size of the maximum defect [36] (in probabilistic terms, this corresponds to the widely adopted weakest-link concept [42, 43]). Therefore, it is vital to estimate the size of the largest material defect that can occur in a material volume.

This analysis employs the "statistics of extremes" [44, 45], which were extensively applied at the end of the 1990s for determining the maximum inclusions in steel. This was mainly achieved by considering observations from two-dimensional (2D) polished sections (PSs) or combining them with measurements of the inclusions at the origin of failure in fatigue specimens. The lessons learned from these studies, which are incorporated into the ASTM E2283 standard [45], are as follows: i) the specimen could be conventionally prepared according to ASTM E45 [46] and scanned using image analysis systems; ii) the "control areas" for PSs (ranging from 0.384 to 100 mm2 in previous studies) had to be as large as possible (typically on the order of 100 mm^2) in order to detect rare particles at the origin of fatigue failure in clean steels; and iii) the largest inclusions in each control area had to be recorded and analyzed with a Gumbel distribution. Quality comparisons of different steels were performed by considering the maximum characteristic value (the modal value for the maximum defect) for a prospective area of 150.000 mm^2 [47].

The measurements prescribed by ASTM E2283 are based on block maxima (BM) sampling. An alternative method for applying the statistics of extremes is the peaks-over-threshold (POT) method [44, 45, 49], which takes into account only the measurements above a threshold value. The POT method was extensively applied by researchers from Sheffield University. It is simple to apply in cases of a large amount of data from automatic measurement systems (no division in blocks/areas is needed) and yields very similar results to the BM method when the assumptions for the underlying parent distribution are compatible with the Gumbel distribution [49].

In a previous study, the concept of "extreme value" statistics for estimating the size of the killer defects in additive manufacturing was applied to data obtained via X-ray µCT [50]. The results showed that the methods developed for inclusions in steels could be successfully applied to three-dimensional (3D) CT scan data by

evaluating the size using Murakami's parameter $\sqrt{area}$ (i.e., the defect area projected onto a plane perpendicular to the applied stress) and that the POT method could be used instead of BM sampling to simplify the analysis and improve the confidence and robustness of the results.

The objective of the present study was to compare the results obtained via complex and expensive nondestructive inspection methods (i.e., µCT) with those attained using simpler and more conventional approaches (i.e., microscopy of PSs, as prescribed by ASTM E2283 [45]), in view of a simple and robust quality assessment of the material. This is done considering the three processes P1-P3 presented in Figure 1. The data quality [51,52] and the prospective cost for analyzing a significant material volume were evaluated for the different techniques.

2. Materials and methods

For this study, AM AlSi10Mg samples were produced via a laser powder-bed fusion process. The chemical composition of the base alloy powder corresponds to DIN EN 1706. A virgin powder was adopted. SLM was performed using an EOS M400 powder-bed machine for manufacturing vertical round bars, which were later machined to form cylindrical fatigue samples without additional heat treatment. No stress-relief was performed, as residual stresses resulted limited owing to the platform pre-heating [17]. Among three batches prepared with varying processes (denoted as P1, P2, and P3), all samples produced in the vertical orientation were considered. The major dimensions of the samples are presented in Table 1. The round bars for P1 and P2 are twice as tall as those for P3; thus, fatigue samples from two different build heights could be extracted. P1 and P2 were produced using the process parameters prescribed by EOS; the only difference was that an improved inert gas recirculation system was used in the powder-bed machine for P2. P3 differed from P2 with regard to two process parameters: the layer thickness (30 µm vs. 60 µm) and the platform pre-heating temperature (165 °C vs. 200 °C as in [53]). The details of the manufacturing parameters adopted are reported in Table 2, together with porosity values evaluated by X-ray micro-CT [17]. Additional information on the materials and processes is presented in previous reports [35, 51].

Defect analysis for the three sample batches was conducted, and the defects were compared among the batches, as shown in Figure 2. The following observations were performed: i) X-ray µCT of gauge sections prior to fatigue testing, ii) scanning electron microscopy (SEM) of the FS after fatigue testing, and iii) optical microscopy of the PSs from the grips after fatigue testing. The number of samples considered for each batch in each observation method is presented in Table 1. The defect size was described by the $\sqrt{area}$ parameter, which allowed the impact of the defects on the fatigue to be simply described regardless of the defect shape [36].

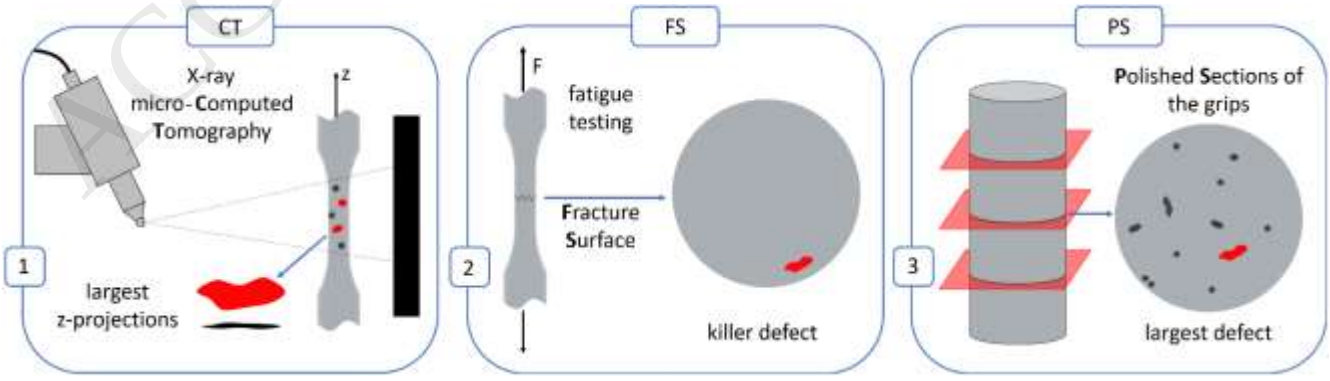

Figure 2: Schematics of the defect investigation methods employed.

Table 1: Main dimensions of the samples investigated.

Process	Number of samples considered			Gauge length (mm)	Gauge diameter (mm)	Grip diameter (mm)
	CT	FS	PS			
P1	3	9	4	13	5.1	11.5
P2	3	8	4	16	6.0	12.0
P3	2	4	4	11	5.5	10.0

Table 2: Processing parameters adopted for the three LB-PBF processes (∗ data not disclosed due to confidentiality agreement with the manufacturer) and porosity values associated.

Process parameter	P1	P2	P3
Laser beam power (W)	1000	1000	*
Energy input (J mm^{-3})	*	*	50
Laser beam focus diameter (µm)	90	90	90
Layer thickness (µm)	60	60	30
Pre-heating temperature of the platform (°C)	200	200	165
Porosity in the samples (%)	0.12 – 0.28	0.15 – 0.38	0.02 – 0.04

2.1. X-ray µCT

X-ray µCT was performed on the gauge sections using a Phoenix V|tome|X m (General Electric). Table 3 presents the main scan parameters. Reconstruction of the scanned volumes was performed using the Phoenix datos|x software (General Electric) to optimize the correction methods for smoothing, beam hardening, ring artefacts, and post-alignment. Defect analysis was conducted using the VG Studio Max 2.2.1 software (Volume Graphics GmbH) using the custom method VGDefX with automatic settings. The defect population was resolved with respect to the position and volume, and $\sqrt{\text{area}}$ data (i.e., the square root of the area projections along the loading direction, which is a standard size parameter provided by the defect analysis software) were derived. These data were then analyzed using appropriate statistical methods for estimating the size of the defects at the fracture origin (see Sec. 4.2).

Table 3: Process parameters employed for µCT (from [50]*).*

µCT process parameter	Value
Voltage (kV)	230
Current (µA)	100
Size of voxel side (µm)	15
Exposure time (ms)	1000
Number of images	1000
Focus–object distance (mm)	67.8
Focus–detector distance (mm)	815

2.2. Fractography

The samples were tested using an Instron E10000 machine in the high-cycle fatigue [16] and low-cycle fatigue regimes [17]. The specimen orientation can influence the distribution of the defects. To avoid this effect, only samples produced in the vertical direction were considered in this study. After the fatigue testing, the fractured samples were prepared for fractography via SEM. The size of the killer defects, which indicated the origin of fatigue failure, was measured and referred to as the critical defect size. The measurements were performed by manually selecting the visible LoF area as in the example of Figure 3b and evaluating the area of the selection using the ImageJ software. The effective equivalent crack size was measured according to the empirical rules commonly adopted for such problems [36].

2.3. Metallography

For optical microscopy, 24 cross sections per batch (four fatigue samples per batch, two grips per sample, three sections per grip) were cut from the grips and prepared via a standard metallographic procedure according to ASTM E2283 [45]. Then, 2D images were obtained using a Leica DMI 5000 M optical light microscope and processed using the Leica Application Suite V5 software. Stitched images were created to record the complete cross section. As the defect detection was performed manually, only the largest visible defects for each cross section were identified and recorded (3–8 defects per cross section). The maximum defect size for each cross section was determined via the Leica software measuring tools and image processing. The same hypotheses about the effective crack size determination reported in Sec. 2.2 were adopted.

3. Results

Table 4 presents the volume of material analyzed, the number of defects sampled, the size of the average and largest defects detected for the three techniques, and the standard deviation of the measurements. Examples of the visual results for the µCT, fractography, and metallographic analysis are shown in Figure 3. The definition of the volumes examined using the metallographic analyses and fractography is not trivial and is discussed in Sec. 3.2.

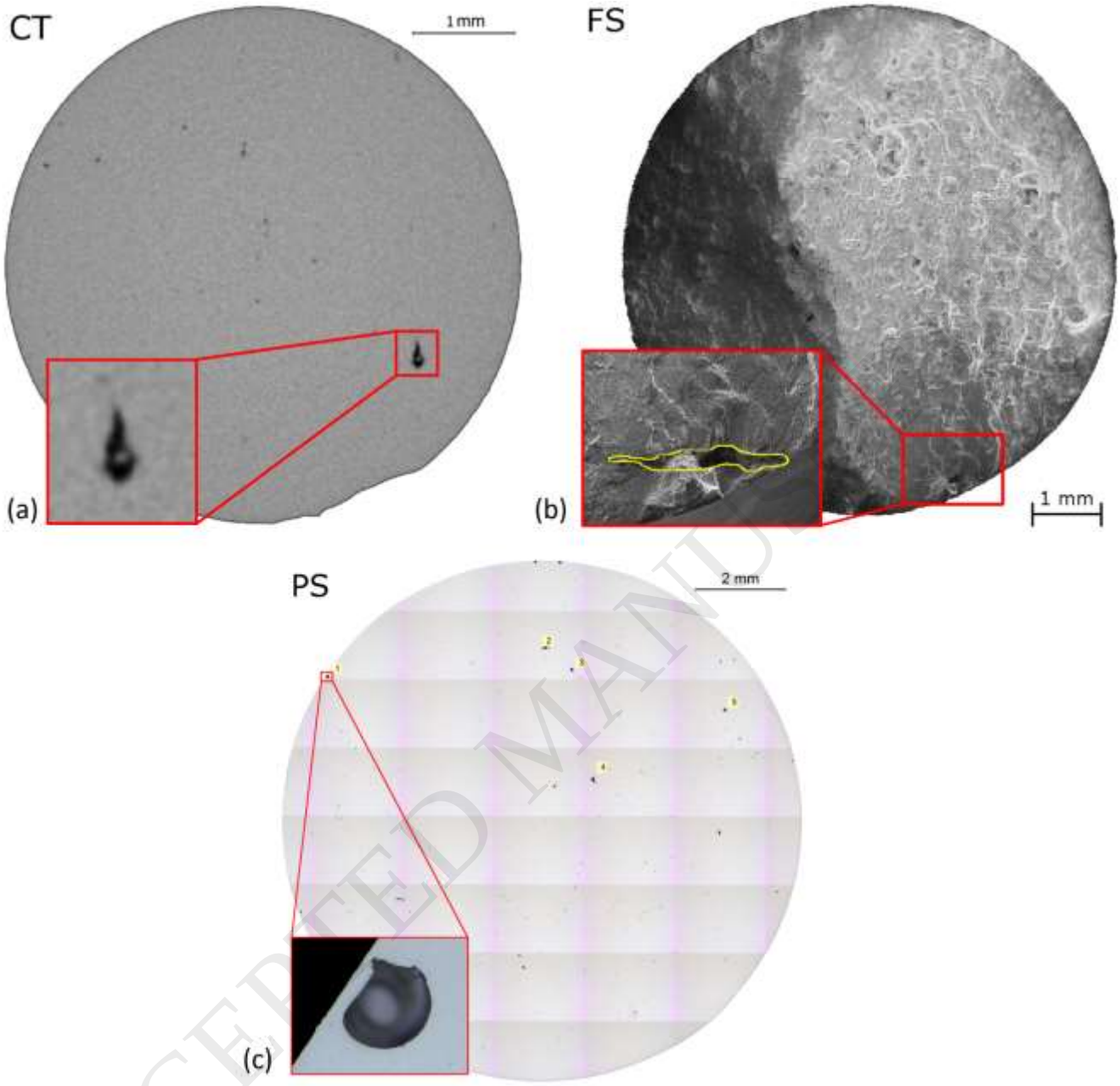

Figure 3: Example of the defects detected by the three analyses: (a) slice obtained via µCT; (b) FS after fatigue testing; (c) PS of one grip cross section.

Table 4: Results of the three analyses for the three processes.

Process	Analysis	Sampled volume (mm^3)	Number of defects	Average defect size (mm)	Largest defect size (mm)	Standard deviation (mm)
P1	CT	3.49×10^3	56738	0.066	0.572	0.030
	PS	2.77×10^2	24	0.111	0.267	0.049
	FS	4.69×10^2	9	0.250	0.361	0.047
P2	CT	4.19×10^3	160609	0.057	0.382	0.014
	PS	1.84×10^2	24	0.068	0.111	0.021
	FS	5.50×10^2	8	0.228	0.307	0.045
P3	CT	2.03×10^3	8940	0.052	0.157	0.010
	PS	6.42×10^1	24	0.034	0.062	0.014
	FS	5.85×10^1	4	0.077	0.110	0.032

3.1. Defect types

The optical investigation of the PSs indicated the presence of three major defect types: porosity, LoF, and pore clustering. In the following, two or more pores are regarded as a cluster if the distance between each other is smaller than the radius of the smallest [36]. Example images are shown in Figure 4. Although infrequent, pore clustering was detected analysing P1, while no clusters were detected considering P2 and P3.

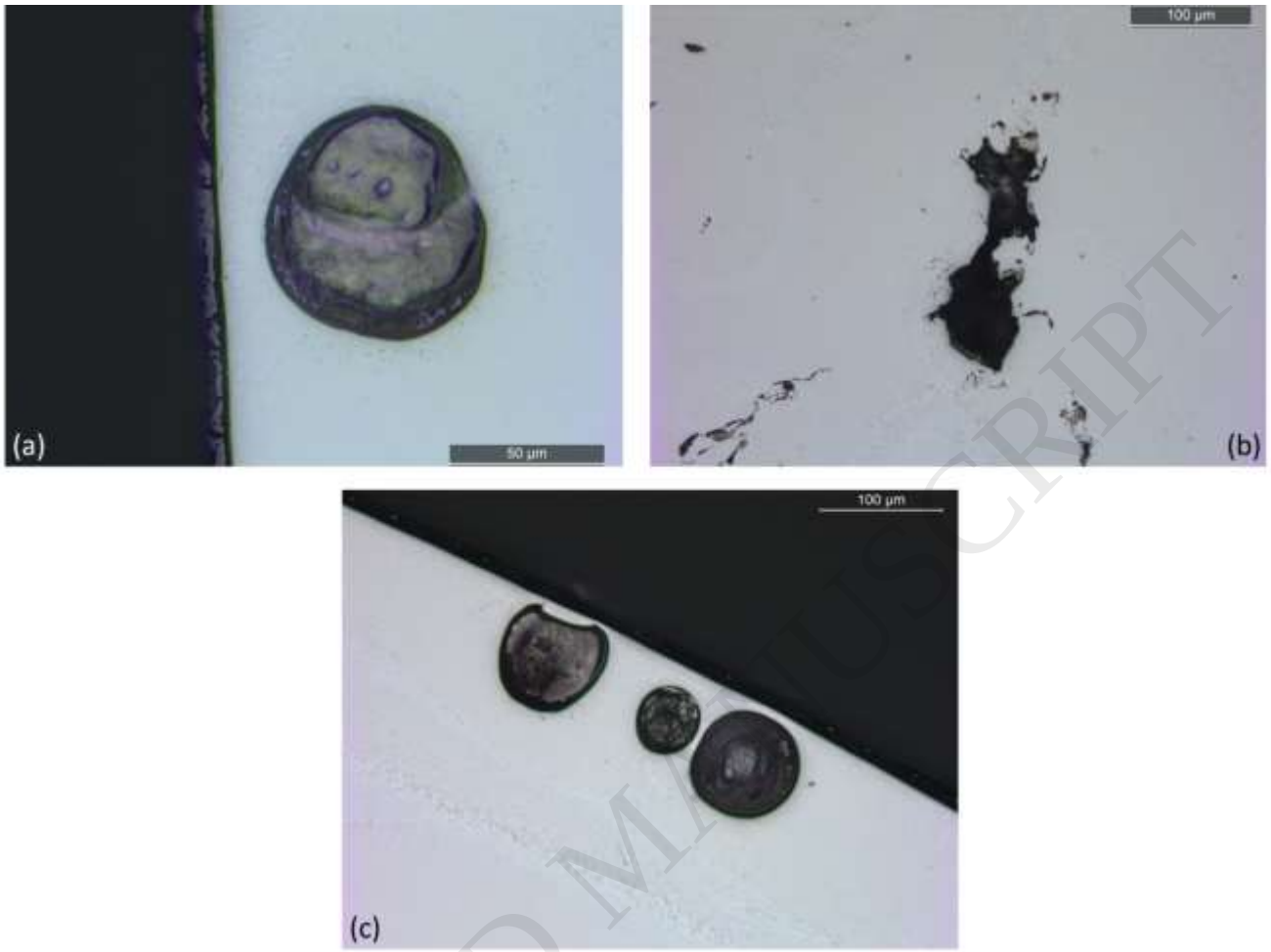

Figure 4: Examples of the defects observed via optical microscopy of the PSs for P1: (a) porosity; (b) LoF; (c) pore cluster.

The gas pores exhibit a typical spherical shape, whereas the LoF is more irregular and is typically elongated in a horizontal plane. Being composed by two or more pores, a cluster also shows some elongation along the building plane. Automatic distinction of the defect types during the analysis of µCT data is not trivial. Therefore, no distinction was made regarding the defects detected via tomography in the present investigation. However, a qualitative distinction based on the defect shape is exploited in Sec. 4.2 to support the choice of the threshold for POT maxima sampling. Regarding the fatigue failures, analysis of the FSs indicated that all failures originated from the LoF at the surface.

3.2. Comparison of measurement methods and inspected volumes

Table 4 shows that the maximum defect size detected via µCT is always larger than those measured via the other two methods. This result is reasonable for the metallographic analyses, but finding defects larger than the killer defects detected on the FS is counterintuitive.

The differences in the size of the maximum defects detected were due to the different material volumes sampled. The volume sampled via µCT corresponds to the total material volume scanned, while this quantity in the metallographic investigation and fractography was approximated by multiplying the control area S_0 for the average defect diameter measured, as shown in Figure 5. Note that pores detected on PSs are more likely sliced

not in the middle of the cross-sections, which causes a systematic underestimation of the defect size. Further discussion is presented in the following subsections. Accordingly, it is important to extrapolate the measurements to the same prospective volume, as explained in Sec. 4.

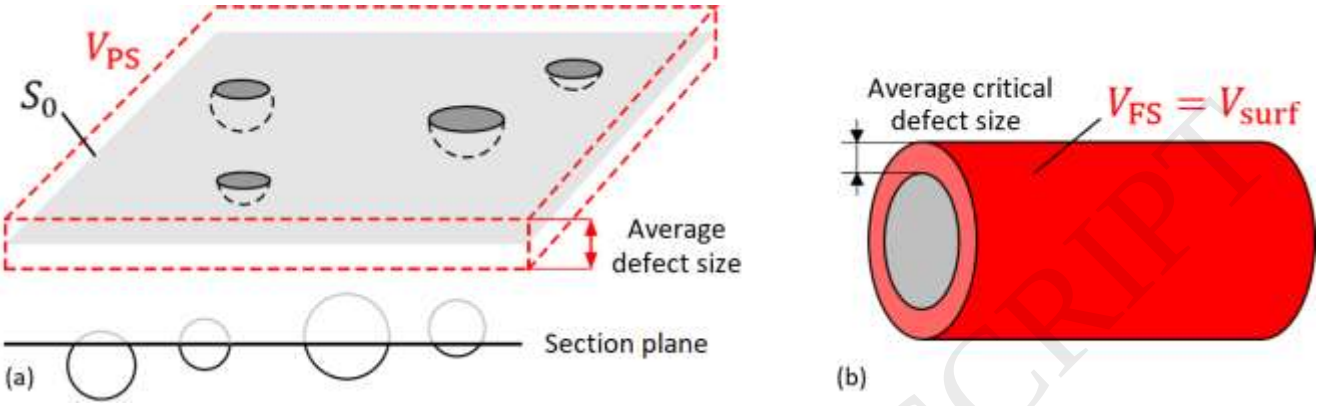

Figure 5: Schematics of the volume analyzed, considering the (a) PSs and (b) investigation of the FSs after fatigue tests (surface gauge volume).

3.2.1 Polished sections

The inference of the distribution of 3D defects from 2D sections is a classical problem in stereology and statistics [54, 55]. The estimation of the distribution of the maximum defect in a volume V_c from data on PSs with a control area S_0 involves the description of the "corpuscle problem" in the statistical analysis [56].

A simple solution to this problem was proposed by Uemura and Murakami [57], who performed numerical simulations of random cuts in a volume containing exponentially distributed spherical defects, as shown in Figure 5a. They defined a conventional control volume V_{PS}, which is calculated as follows:

$$V_{PS} = S_0 \cdot h_{\text{mean}}, \tag{1}$$

where h_{mean} is the average size of the defect sections recorded in the 2D analysis (see the schematic in Figure 5a). The overall volume investigated using the PS, as shown in Table 4, was calculated by multiplying V_{PS} by the number of maximum defects sampled (i.e., 24). Takahashi and Shibuya analyzed a theoretical model of Wicksell's problem under the hypothesis that the size distribution of random spheres follows a generalized gamma distribution [58] and reported a reasonable approximation of an equivalent volume (see Eq. (1)) compared to theoretical results. This approximation was adopted for the present analysis, although more complex models accounting for the non-spherical shape of LoF defects (the most detrimental ones for the three processes investigated as highlighted by fractographies [16]) can slightly improve the volume evaluation.

3.2.2 Fracture surfaces

Considering fatigue, failure occurs at the largest defect or inhomogeneity present in the most stressed volume [36]. In reality, knowing the defect size and applied stress is not sufficient to describe the fatigue strength of parts. Defects located at or close to the surface are more detrimental than internal ones, which is why most fatigue failures in AM materials start from surface defects [24, 29, 35, 60]. A robust assessment of the criticality

of a defect can be performed by determining the stress intensity factor (SIF). The simplest formulation of the SIF due to defects is that based on the $\sqrt{\text{area}}$ parameter, which was proposed by Murakami [60]:

$$K = Y\, S \sqrt{\pi \sqrt{\text{area}}}. \tag{2}$$

According to this formulation, the SIF for a surface defect is 30% higher than that for an internal one of the same size and subjected to the same stress S, as the boundary correction factor is $Y = 0.65$ for surface defects and $Y = 0.5$ for internal defects.

Romano et al. [16] demonstrated that, in the majority of cases, the killer defect of a cylindrical fatigue sample is the largest defect inside a surface volume V_{surf}. Using a calculation similar to that presented in Eq. (1), this volume can be approximated by multiplying the outer surface area of the gauge section by a constant depth, which is estimated according to the average size of the killer defects within this batch (see Figure 5b). The overall volume investigated via FS analysis presented in Table 4 was therefore calculated by multiplying the number of specimens investigated (see Table 1) by the volume $V_{FS} = V_{\text{surf}}$.

4. Data analysis and extrapolation

The distribution of the maximum value Z_n from a set of n individual values Z described by a cumulative distribution function F_Z is [61]

$$F_{Z_n} = [F_Z]^n. \tag{3}$$

The modal value of F_{Z_n} is called the characteristic maximum value over n extractions (i.e., the value that, on average, is most frequently exceeded every n extractions) and is the value of *Z* associated with a return period $T = n$. The cumulative probability of this quantity is described as follows:

$$F = 1 - \frac{1}{T} = 1 - \frac{1}{n}. \tag{4}$$

There are two different approaches for addressing the statistics of extremes with appropriate sampling strategies—POT and BM—as schematically shown in Figure 6. On the one hand, BM is the most common and simple approach, which consists in dividing the specimen into several equivalent sub-volumes and selecting the maximum value contained in each sub-volume. On the other hand, POT is naturally applied to automatic measurements as those obtained by µCT and consists in considering all the values above a given threshold *u*, so that no important information is lost. In general, POT estimates are more precise than those obtained by BM [49]. The application of these approaches to the data collected is described in the following subsections.

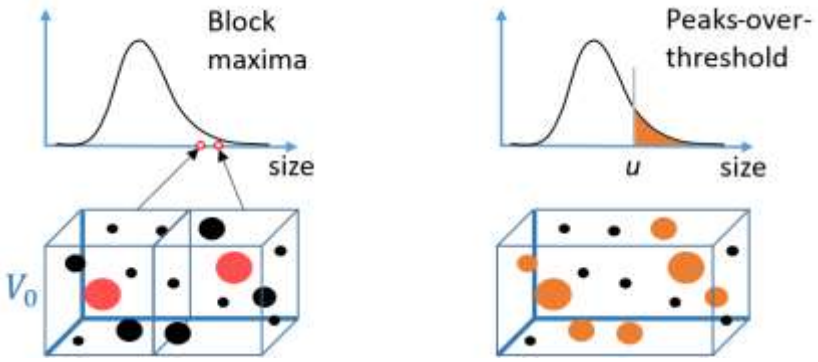

Figure 6: Schematics of the BM and POT maxima sampling strategies (adapted from [50]*).*

4.1. Analysis of PS data—BM approach

The distribution of the extreme values $X \equiv Z_n$ $(n \to +\infty)$ can be well approximated by a generalized extreme value distribution [44]. The X data can be sampled by recording the maximum defects in a given material volume V_0. If the distribution F_Z has an exponential tail, the distribution of $X = Z_n$ is described by the largest extreme value distribution (LEVD) [61]:

$$F_{\max,V_0}(x) = \exp\left(-\exp\left(-\frac{x-\lambda}{\delta}\right)\right), \tag{5}$$

where the parameters λ and δ (called the location and scale parameters, respectively) can be estimated using various data analysis methods [62]. The p-percentile of the distribution is

$$x_p = \lambda - \delta \cdot \log[-\log(p)]. \tag{6}$$

Given a prospective component volume (or, in general, a material volume) of interest, the return period of the characteristic maximum defect is

$$T = V_c/V_0. \tag{7}$$

By exploiting the relationship between the cumulative probability and the return period (Eq. (4)), the characteristic maximum value $\hat{x}_T$ can be obtained as follows:

$$\hat{x}_T = \hat{\lambda} - \hat{\delta} \cdot \log\left[-\log\left(1-\frac{1}{T}\right)\right] \approx \hat{\lambda} + \hat{\delta} \cdot \log(T), \tag{8}$$

where $\hat{\lambda}$ and $\hat{\delta}$ are the estimates for the two distribution parameters.

Figure 7a shows the LEVD probability plot for P1, which compares the distributions of the pores and LoF detected in the PSs. The image shows that the two defect types belong to different LEVDs, and the LoF distribution appears to be more critical with regard to size. The size of the pore clusters is similar to that of the LoF but, because of the small number of measurements, a reliable statistical description cannot be derived. Figure 7b indicates that a unique LEVD cannot provide a good description of various defect types.

This observation is contradictory to the requirements of the defect assessment guidelines of ASTM 2283, which can only be applied to a single defect type. A competing risk model can be adopted for describing the prospective distribution of the maximum defect if different types of particles/inhomogeneities are present and recognized

[63]. Moreover, the data fitting with multiple defect types requires a suitable model description and additional data points, as in the approach presented in [63, 64].

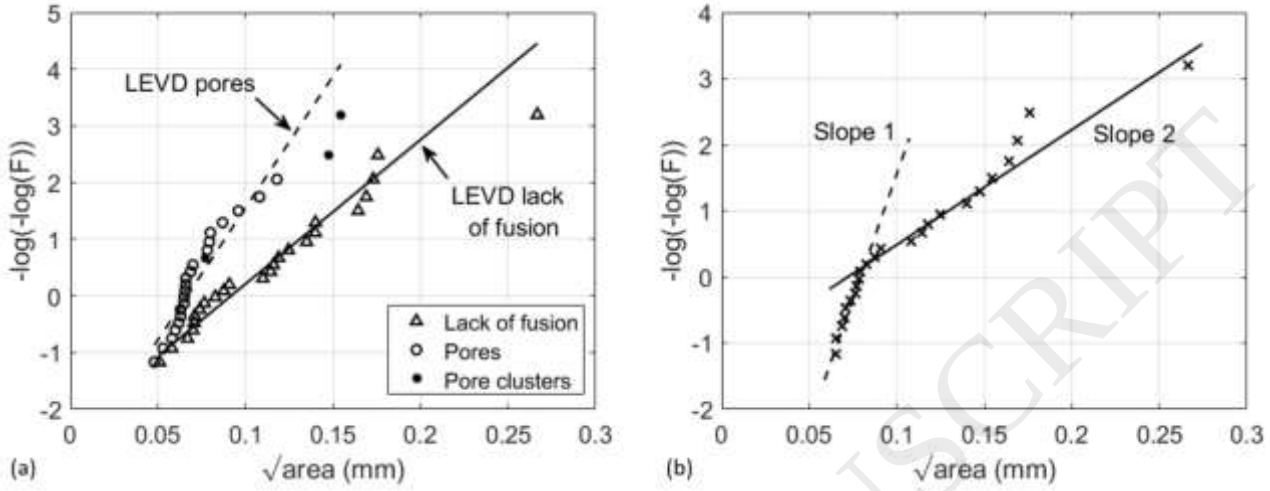

Figure 7: LEVD of the PS data determined for P1 depicted in a Gumbel probability plot: (a) distinction according to the type of the maximum defect; (b) 24 maxima measured with no defect-type distinction.

Therefore, the analysis of the PSs was performed by separating the pores from the LoF. Despite the different layer thickness and platform pre-heating temperature adopted, the largest defects on each PS were mainly the LOF for both P2 and P3. The evidence of LoF showing the largest size for all processes explains why this defect type was found at the origin of all fatigue failures. A separate LEVD was then fitted to the 24 maxima for both processes, and the most detrimental defect type (LOFs for the three series) was considered for the extrapolation.

The LEVD parameters and the characteristic maximum values are presented in Table 5. The extrapolations were performed with respect to the surface gauge volumes $V_c = V_{\mathrm{FS}}$, and the return period was calculated by substituting $V_{PS} = V_0$ into Eq. (7) (the volume V_{PS} corresponds to the control volume of each of the 24 maximum defects considered). In Sec. 5, these results are compared to the measurements performed on the FSs to evaluate the effectiveness of PS analysis for critical defect size estimation.

Table 5: Parameters of the LEVD distribution of defects from the PS data for the BM approach (see Eqs. (5) and (8)).

Process	V_{PS} (mm^3)	λ (mm)	δ (mm)	$\hat{x}_T$ (mm)
P1	1.16×10^1	0.089	0.038	0.147
P2	7.68×10^0	0.058	0.016	0.094
P3	2.67×10^0	0.028	0.011	0.047

4.2. Analysis of µCT data—POT approach

An alternative approach to BM is the POT method, in which only the data above a sufficiently high threshold u are analyzed [48]. If the values $z > u$ are considered (i.e., the values exceeding the threshold u), the data are described by a truncated distribution:

$$F_Z(z)^{[u]} = \frac{F_Z(z) - F_Z(u)}{1 - F_Z(u)}. \qquad (9)$$

The distribution of the exceedances $X \equiv Z: X > u$ can be approximated as a generalized Pareto distribution [44, 45]. In most practical cases, the tail of the original distribution is exponential; therefore, the exceedances X can be described by a negative exponential distribution F_{exc}:

$$F_{\mathrm{exc}}(x) = 1 - \exp\left(-\frac{x-u}{\sigma}\right), \tag{10}$$

where σ is the mean value of the exceedances $(X-u)$. The p-percentile is

$$x_p = u - \sigma \cdot \log(1-p). \tag{11}$$

If N_u defects larger than u are collected in a volume V_0, the return period of the maximum defect in a volume V_c is

$$T = N_u \cdot \frac{V_c}{V_0} = \rho \cdot V_c, \tag{12}$$

where ρ is the volumetric density of the defects larger than u. The characteristic size of the maximum defect in V_c is then

$$\hat{x}_T = u + \hat{\sigma} \cdot \log(T), \tag{13}$$

where $\hat{\sigma}$ is the estimate for the mean value of the exceedances.

This method is suitable for analyzing CT measurements, as it allows small defects (which have a small influence on the material properties) to be neglected and a precise and robust fit of the upper tail of the data with high confidence to be obtained [50, 65]. Moreover, problems related to multiple defect types can be easily avoided by choosing a value u that is only exceeded by the most detrimental defect type.

This is clearly observed in Figure 8a, which illustrates the defect shape according to the µCT data for P1. Regarding the sphericity of the defects, it is clear that the small measurements are pores (sphericity above an empirical value of approximately 0.5), whereas the values above 150 µm (whose position is depicted in Figure 8b) have a more elongated shape because of the LoF. Here, the sphericity indicates the ratio between the surface area of a sphere with the same volume as the defect (V_{def}) and the surface of the defect (S_{def}):

$$\mathrm{sphericity} = \frac{3}{R_{\mathrm{sphere}}} \frac{V_{\mathrm{def}}}{S_{\mathrm{def}}}. \tag{14}$$

A negative exponential probability plot of the data clearly reveals that, above this threshold, the data become almost linear (Figure 9a) and can be described by an exponential distribution (Figure 9b), as previously reported [50].

The same procedure was conducted for the defect data from P2 and P3. The exceedances were fitted by a negative exponential distribution, as shown in Figure 9b. The characteristic maximum defect size $\hat{x}_T$ was estimated using the POT approach (Eqs. (12) and (13)) considering a material volume of $V_c = V_{\mathrm{surf}}$, as shown in Table 6.

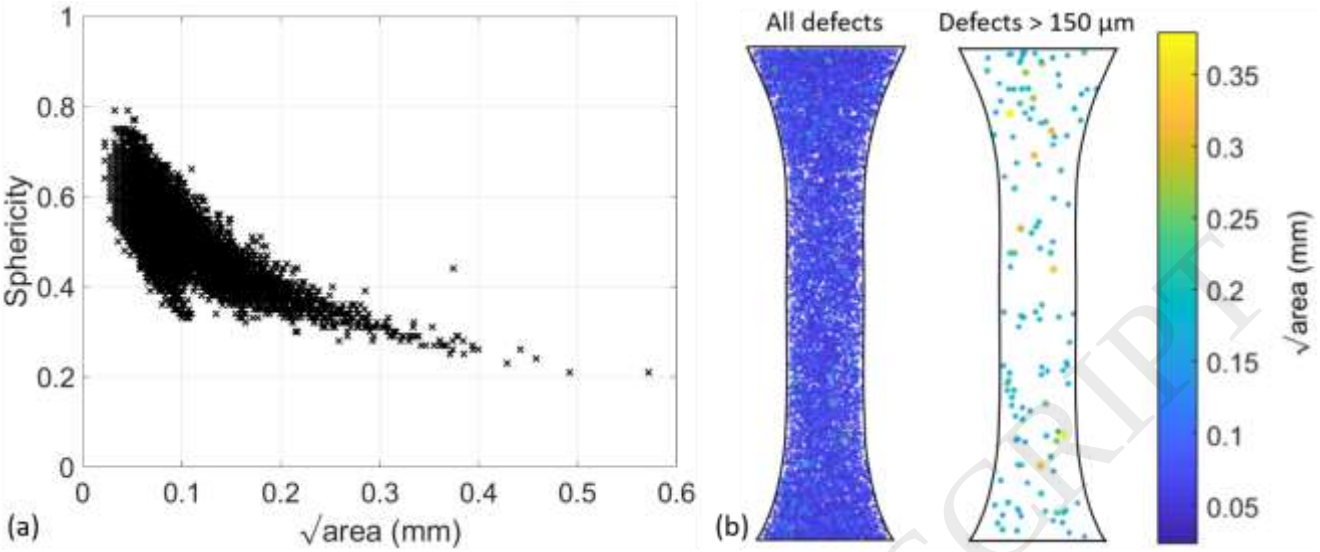

Figure 8: µCT results for P1: (a) decrease of the sphericity with respect to the defect size, considering all the data measured; (b) homogeneous distributions of the defects (left) and exceedances (right) detected in one of the specimens.

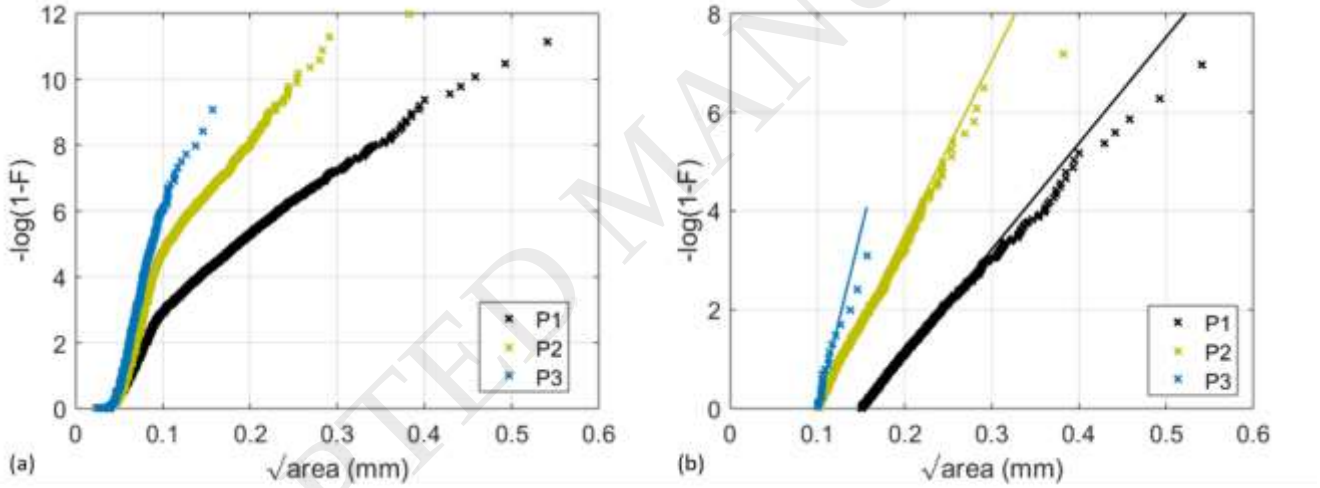

Figure 9: Distributions of the defect sizes measured via µCT and evaluated using a negative exponential probability plot: (a) comparison of all the data; (b) fits for the exponential distributions of exceedances above the selected threshold.

Table 6: Parameters of the negative exponential distribution of defects from µCT data based on the POT approach (see Eqs. (10), (12), and (13)).

Process	V_{CT} (mm^3)	u (mm)	N_u	ρ (defects/mm^3)	σ (mm)	$\hat{x}_T$ (mm)
P1	3.49×10^3	0.150	1334	0.383	0.049	0.297
P2	4.19×10^3	0.100	1319	0.315	0.021	0.187
P3	2.03×10^3	0.100	21	0.010	0.014	0.074

5. Discussion

5.1. Comparison and estimation of critical defect size

The characteristic maximum defect sizes for the volume V_{surf} estimated using the PS and CT methods are presented in Table 5 and Table 6, respectively. To investigate the quality of the extrapolation, it is important to compare the predictions with the defects at the origin of failure with regard to the distribution.

Using Eq. (3), the distribution of the maximum defect size in V_{surf} can be estimated as shown in Eqs. (15) and (16) for the BM and POT methods, respectively:

$$F_{\max,V_{\mathrm{surf}},PS}(x) = \left[F_{\max,V_{\mathrm{PS}}}\right]^{T} \tag{15}$$

$$F_{\max,V_{\mathrm{surf}},CT}(x) = \left[F_{\mathrm{exc}}(x)\right]^{T}, \tag{16}$$

where *T* is calculated using Eq. (7) for BM and Eq. (12) POT.

Figure 10a presents a comparison of the results obtained for P1 in the LEVD probability plot. As shown, both the PS and CT estimates are close to the experimental distribution of the killer defects, and the slope of the data is correctly determined. However, the analysis of the µCT data provides a conservative estimation of the critical defect size, whereas the analysis of the PS data yields non-conservative values. Moreover, µCT has the further advantage of being a non-destructive technique.

Figure 10b presents the defect sizes obtained via all the methods for the three processes. The characteristic maximum defect and 90% scatter band reported for the PS and CT estimates refer to the volume V_{FS} for the respective process (see Table 4).

The results show that the extrapolation to V_{surf} allows the prediction of the progressive improvement of the fatigue properties from P1 to P3 (see Figure 10b) based on both metallographic investigation and µCT. The sizes of the critical defects estimated according to the µCT data appear consistent and robust, with a slight but conservative overestimation for P1. The estimation of a critical defect size larger than the experimental one allows a smaller applicable load to be used in the Kitagawa-Takahashi diagram or the estimation of a shorter fatigue life via fatigue crack growth simulations. In contrast, the estimates obtained from PSs are less robust and generally non-conservative.

Underestimation of the critical defect sizes could also arise from considering defect types that do not correspond to killer defects. Even though multiple defect types were detected, all the fatigue failures were caused by the LoF in the surface volume. On one hand, it was difficult to automatically distinguish pores from LoF via µCT analysis. On the other hand, Figure 7 clearly shows that a proper choice of the threshold for POT maxima sampling (i.e., 150 µm for P1) ensures that defect sizes that do not correspond to the killer defect type are nearly completely ignored. Considering clusters of pores, it is possible that small gaps between the defects are not recognised as base material and therefore a unique large pore is detected. This must be evaluated on a case-by-case basis. Considering P1, the probability of measuring non-LoF defects with a size larger than 150 µm is expected to be small. In fact, the largest pore cluster detected on PSs having a gap smaller than two times the voxel size used for µCT measured approximately 100 µm. Moreover, a few incorrect measurements do not sensibly affect the statistical analysis performed on all LoF data. This issue is even less likely considering P2 and P3, as no clusters of pores were detected.

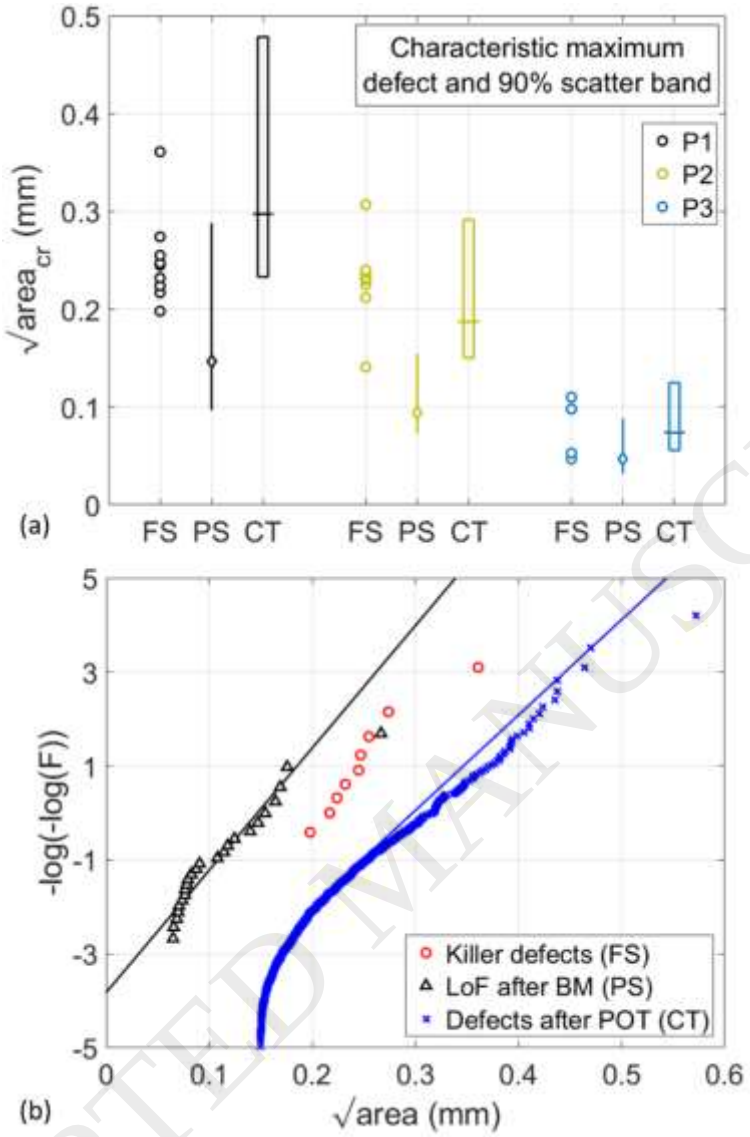

Figure 10: Experimental critical defect size (FS) compared with extreme value estimates based on CT or PS data: (a) LEVD probability plot for P1; (b) overview of the three processes.

5.2. Cost and efficiency

Another focal point of this study is the comparison of the costs and efficiency of X-ray µCT and metallography, which are the most frequently used methods for defect analysis. For this, the time required to perform both investigations in this study was estimated according to the laboratory infrastructure available. The estimates are based on an experienced operator using fully functional equipment. Table 7 presents the time needed for all the analysis steps of the respective methods. All the data are based on the procedure, equipment, and material adopted for the present investigation. The time includes both man hours (i.e., time needed for an operator to conduct or actively supervise the job) and analysis time/waiting time (i.e., process time that does not require the attendance or supervision of the operator).

Table 7: Comparison of X-ray µCT and PS microscopy with regard to man hours and analysis time needed to complete the defect analysis of one sample and a batch of four samples. X-ray µCT analyzes the gauge section, while PS microscopy considers six cross sections from

the grips per sample. Regarding defect analysis, X-ray µCT considers all defects above a predefined threshold, while PS microscopy only considers the three largest defects per cross section.

X-ray µCT			PS microscopy		
Step	Man hours (h)	Analysis/ waiting time (h)	Step	Man hours (h)	Analysis/ waiting time (h)
Preparation	0.33	0.00	Cutting of six microsections	0.60	0.00
Scanning process	0.00	2.50	Cold embedding (three microsections per embedded sample)	0.08	0.00
Reconstruction	0.20	0.50	Curing time of resin	0.00	8.00 (only once)
File opening	0.20	0.50	Manual mechanical grinding	1.00	0.00
Software detection and calculation of defect sizes	0.00	1.50	Semiautomatic mechanical polishing	0.25	0.00
			Optical light microscopy – image capture	1.50	0.00
			Optical light microscopy – Interpretation and calculation of defect sizes	0.60	0.00
Total per sample	0.73	5.00	Total per sample	4.03	8.00
Total per batch (i.e., three samples)	2.19	15.00	Total per batch (i.e., four samples)	16.12	8.00

As discussed in Section 4, the most convenient data-acquisition method was adopted for each investigation technique, i.e., POT maxima sampling for the µCT data and BM sampling for the PS. This led to a significant difference in the number of sampled defects between the CT and PS, as shown in Table 4.

The larger number of defects sampled by µCT is also indicated by the longer analysis time (15 h per batch). Apart from this, the amount of man hours needed (usually for initiating the processing) is small overall (2.19 h per batch) compared with that for PS microscopy (16.12 h per batch). This is mainly due to the lack of automation of the metallographic preparation and the use of light microscopes.

With regard to financial expenses, a simple cost assessment was performed for the analysis conducted in an internal facility or contracted externally. Quotation of investment and maintenance for CT refer to the specific lab location (i.e., Europe) and machine. Although limited variations may be expected, the results and comments are not expected to be sensibly affected. Although the costs reported herein are only applicable for this study, they showcase various aspects and focal points to consider for the selection of a reliable and profitable method in an industrial setting.

For an internal laboratory, the costs for investment C_i and maintenance/consumables C_c are evenly distributed along the lifetime L, which is assumed to be 10 years in both cases. The internal cost per batch C_b was calculated as follows:

$$C_b = \left(\frac{C_i}{L} + C_c\right) \cdot \frac{T_b}{N_h} + C_m \cdot T_m, \tag{17}$$

where T_b is the time needed to analyze one batch of material, N_h is the availability of the machines per year, C_m is the hourly wage of an experienced technician, and T_m is the amount of man hours needed for the analyses, as reported in Table 7. The values of C_m serve as a reference and assume a CT technician wage 25% higher than the industry standard owing to the additional training needed. The availability N_h was assumed to be higher for CT scanning than for PS microscopy, as an important part of the tomography, reconstruction, and defect analysis can be performed at night without the presence of a technician.

The investment cost and the maintenance/consumables cost for metallography were estimated by considering the standard equipment needed, i.e., the cutting machine, grinder, polisher, cold mounting equipment, optical microscope, workstation, and application software. For µCT, the costs are based on the Phoenix V|tome|X m (General Electric), workstation, and VG Studio Max 3.2 software. The cost for outsourcing was estimated according to the typical prices of specialized labs on the market in 2018 (costs excluding value added tax).

As both methods consider significantly differing volumes, which can be investigated to a reasonable extent of experimental time and effort, the cost per unit volume C_v was also determined. C_v was calculated by dividing C_b by the overall volume investigated (see Table 4). The cost assessment of µCT for P3 was performed by increasing the volume investigated by 50%, i.e., considering the analysis of three samples, as for P1 and P2. Table 8 compares the aforementioned costs.

Table 8: Estimated costs for defect analysis via PS microscopy and CT scanning, either performed by an internal laboratory or outsourced to a third party.

	Internal lab		Outsourced contract	
	PS	CT	PS	CT
Investment C_i (€)	131k	650k	-	-
Maintenance + consumables C_c (€/year)	8.9k	20.0k	-	-
Machine availability N_h (h/year)	1500	2000		
Time per batch T_b (h)	24.12	17.19	-	-
Technician wage C_m (€/h)	80	100		
Man hours T_m (h)	16.12	2.19	-	-
Cost per batch C_b (€)	1643	950	4500–6500	1800–2700
Cost per unit volume C_v (€/mm^3) – P1	5.93	0.27	16.25–23.47	0.52–0.77
Cost per unit volume C_v (€/mm^3) – P2	8.93	0.22	24.46–35.33	0.43–0.64
Cost per unit volume C_v (€/mm^3) – P3	25.59	0.31	46.73–67.50	0.89–1.33

Although the estimated costs per batch significantly vary with respect to the technician wage, the results show a relatively small difference in the costs for internal labs between the two procedures adopted. The estimated cost for analyzing 24 PSs is approximately twice that for performing µCT on three samples.

The estimates for the PS case can be improved by investigating a larger volume, i.e., a volume on the order of that evaluated via µCT. Nevertheless, the cost comparison per unit volume reveals that, when the volume to be investigated increases, PS becomes less profitable, whereas µCT remains cost-effective. These results agree with those previously reported for SLM Ti-6Al-4V [51] and contradict the conclusion of P. Wang et al. [52], who stated that PS microscopy observations are cheaper and more accurate than µCT scans.

With the improvement of the material quality, the cost per unit volume for PS increases to a greater degree than that for µCT. This is because the average defect size—and therefore the equivalent volume investigated via 2D analysis—decreases. For this reason, a larger sectional area has to be investigated via PSs. Finally, it is worth noting that inspection via X-ray µCT becomes less effective when applied to high-density materials or in the presence of very small defect sizes. For this reason, a larger sectional area has to be investigated via PSs. Finally,

it is worth noting that inspection via X-ray µCT becomes less effective when applied to high-density materials or in the presence of very small defect sizes. These limits and others are well known and are described in detail specifically for additively manufactured materials in [24] and more generally for materials sciences in [66]. In these cases, PS analysis might result a simpler and more cost-effective process but with potentially useful 3D information lost. Similar considerations can be drawn regarding surface quality assessment for additively manufactured materials in the net-shape condition [67,68] , which is why standardized procedures are being presented, see for example [69].

6. Conclusions

The quality of three batches of AlSi10Mg produced by SLM was investigated with regard to fatigue strength by evaluating the distribution of manufacturing defects. The defect distributions were investigated via optical microscopy of the PSs and X-ray µCT. The results thus obtained were then compared to the size of critical defects measured on FSs after applying statistics of extreme to evaluate consistent material volumes.

The following conclusions are drawn.

- Both methods were able to predict the variation in critical defect size between the three batches and can therefore be used for a qualitative comparison of fatigue strength.
- The application of statistical methods to estimate the critical defect size of fatigue samples yielded robust results when based on µCT data, whereas non-conservative estimates were obtained via metallographic analyses.
- To obtain precise estimates, it is necessary to investigate a sufficient material volume to correctly describe the distribution of the critical defect type.
- µCT appears to be preferable over metallographic analysis because it allows the quick investigation of larger material volumes and the measurement of the defects in their most critical section. Moreover, µCT has the further advantage of being a non-destructive technique.
- A comparison of the work and analysis effort between the methods revealed that metallographic inspection requires a larger amount of man hours, while the cost per batch is comparable to that of µCT. Moreover, µCT becomes more cost-effective with the increase of the investigated material volume.
- The cost difference between PS and µCT becomes even larger in the case of outsourcing, with metallography being more expensive than µCT even for relatively small material volumes.

Acknowledgements

The authors thank RUAG Space for providing the P1 and P2 samples.

Part of the study was performed during S. Romano's PhD, which was partially supported by ESA through Networking Partnering Initiative (NPI) No. 4000120615/17/NL/MH. The authors thank two anonymous reviewers for valuable comments.

References

[1] T. Wohlers, I. Campbell, O. Diegel, others, Wohlers Report 2018, 2018.

[2] B. Sagel, Premium AEROTEC begins serial production of printed titanium components, (2016). https://www.premium-aerotec.com/en/media/press-releases/premium-aerotec-begins-serial-production-of-printed-titanium-components/ (accessed December 12, 2018).

[3] AVIO, Successfully tested the M10-methane engine prototype, (2018). http://www.avio.com/en/press-release/successfully-tested-the-m10-methane-engine-prototype/ (accessed December 12, 2018).

[4] THALES, Metal 3D printing: THALES creates a global centre of expertise in Morocco, (2017). https://www.thalesgroup.com/en/worldwide/aerospace/press-release/metal-3d-printing-thales-creates-global-centre-expertise-morocco (accessed December 12, 2018).

[5] RUAG, Additive manufacturing partnership for space applications, (2018). https://www.ruag.com/en/news/additive-manufacturing-partnership-space-applications (accessed December 12, 2018).

[6] OHB, OHB awarded ESA contract for the development of 3D-printed satellite components and instruments, (2018). https://www.ohb.de/en/news/ohb-awarded-esa-contract-for-the-development-of-3d-printed-satellite-components-and-instruments/ (accessed December 12, 2018).

[7] BOEING, Oerlikon and Boeing to Collaborate in Additive Manufacturing Work, (2018). https://boeing.mediaroom.com/2018-02-20-Oerlikon-and-Boeing-to-Collaborate-in-Additive-Manufacturing-Work (accessed December 12, 2018).

[8] SPACEX, SPACEX launches 3D-printed part to space, creates printed engine chamber, (2014). https://www.spacex.com/news/2014/07/31/spacex-launches-3d-printed-part-space-creates-printed-engine-chamber-crewed (accessed December 12, 2018).

[9] Aerojet Rocketdyne, Aerojet Rocketdyne is leading the industry in designing and building aerospace components using 3-D printing technology, (n.d.). http://www.rocket.com/additive-manufacturing (accessed December 12, 2018).

[10] AIRBUS, First titanium 3D-printed part installed into serial production aircraft, (2017). https://www.airbus.com/newsroom/press-releases/en/2017/09/first-titanium-3d-printed-part-installed-into-serial-production-.html (accessed December 12, 2018).

[11] ArianeGroup, ArianeGroup continues ETID hot-fire tests with first full-scale 3D-printed combustion chamber injector head, (2018). https://www.ariane.group/wp-content/uploads/2018/11/ArianeGroup_continue_ETID_tests_24112018.pdf (accessed December 12, 2018).

[12] J. Günther, D. Krewerth, T. Lippmann, S. Leuders, T. Tröster, A. Weidner, et al., Fatigue life of additively manufactured Ti–6Al–4V in the very high cycle fatigue regime, Int. J. Fatigue. (2016). doi:10.1016/j.ijfatigue.2016.05.018.

[13] T. DebRoy, H.L. Wei, J.S. Zuback, T. Mukherjee, J.W. Elmer, J.O. Milewski, et al., Additive manufacturing of metallic components – Process, structure and properties, Prog. Mater. Sci. 92 (2018) 112–224. doi:https://doi.org/10.1016/j.pmatsci.2017.10.001.

[14] K. Kempen, L. Thijs, E. Yasa, M. Badrossamay, W. Verheecke, J.P. Kruth, Process Optimization and micostructural analysis for Selective Laser Melting of AlSi10Mg, Solid Free. Fabr. (2011) 484–495.

[15] C. Weingarten, D. Buchbinder, N. Pirch, W. Meiners, K. Wissenbach, R. Poprawe, Formation and reduction of hydrogen porosity during selective laser melting of AlSi10Mg, J. Mater. Process. Technol. 221 (2015) 112–120. doi:https://doi.org/10.1016/j.jmatprotec.2015.02.013.

[16] S. Romano, A. Brückner-Foit, A.D. Brandão, J. Gumpinger, T. Ghidini, S. Beretta, Fatigue properties of AlSi10Mg obtained by additive manufacturing: Defect-based modelling and prediction of fatigue strength, Eng. Fract. Mech. 187 (2018) 165–189. doi:10.1016/j.engfracmech.2017.11.002.

[17] S. Romano, L. Patriarca, S. Foletti, S. Beretta, LCF behaviour and a comprehensive life prediction model for AlSi10Mg obtained by SLM, Int. J. Fatigue. 117 (2018) 47–62. doi:10.1016/j.ijfatigue.2018.07.030.

[18] Y. Xue, A. Pascu, M.F. Horstemeyer, L. Wang, P.T. Wang, Microporosity effects on cyclic plasticity and fatigue of LENS^{TM}-processed steel, Acta Mater. 58 (2010) 4029–4038. doi:10.1016/j.actamat.2010.03.014.

[19] S. Beretta, S. Romano, A comparison of fatigue strength sensitivity to defects for materials manufactured by AM or traditional processes, Int. J. Fatigue. 94 (2017) 178–191. doi:10.1016/j.ijfatigue.2016.06.020.

[20] A. Yadollahi, N. Shamsaei, Additive Manufacturing of Fatigue Resistant Materials: Challenges and Opportunities, Int. J. Fatigue. 98 (2017) 14–31. doi:10.1016/j.ijfatigue.2017.01.001.

[21] W.E. Frazier, Metal additive manufacturing: A review, J. Mater. Eng. Perform. 23 (2014) 1917–1928. doi:10.1007/s11665-014-0958-z.

[22] H. Galarraga, D.A. Lados, R.R. Dehoff, M.M. Kirka, P. Nandwana, Effects of the microstructure and porosity on properties of Ti-6Al-4V ELI alloy fabricated by electron beam melting (EBM), Addit. Manuf. 10 (2016) 47–57. doi:https://doi.org/10.1016/j.addma.2016.02.003.

[23] R.A. Livings, E.J. Biedermann, C. Wang, T. Chung, S. James, J.M. Waller, et al., Nondestructive Evaluation of Additive Manufactured Parts Using Process Compensated Resonance Testing, in: ASTM Sel. Tech. Pap., Washington, 2018.

[24] A. du Plessis, S.G. le Roux, Standardized X-ray tomography testing of additively manufactured parts: A round robin test, Addit. Manuf. 24 (2018) 125–136. doi:https://doi.org/10.1016/j.addma.2018.09.014.

[25] A. Thompson, I. Maskery, R.K. Leach, X-ray computed tomography for additive manufacturing: a review, Meas. Sci. Technol. 27 (2016) 072001. doi:http://dx.doi.org/10.1088/0957-0233/27/7/072001.

[26] P. Li, D.H. Warner, A. Fatemi, N. Phan, Critical assessment of the fatigue performance of additively manufactured Ti-6Al-4V and perspective for future research, Int. J. Fatigue. 85 (2016) 130–143. doi:10.1016/j.ijfatigue.2015.12.003.

[27] M. Seifi, A. Salem, J. Beuth, O. Harrysson, J.J. Lewandowski, Overview of Materials Qualification Needs for Metal Additive Manufacturing, Jom. 68 (2016) 747–764. doi:10.1007/s11837-015-1810-0.

[28] S. Leuders, M. Thöne, A. Riemer, T. Niendorf, T. Tröster, H.A. Richard, et al., On the mechanical behaviour of titanium alloy TiAl6V4 manufactured by selective laser melting: Fatigue resistance and crack growth performance, Int. J. Fatigue. 48 (2013) 300–307. doi:10.1016/j.ijfatigue.2012.11.011.

[29] P. Edwards, M. Ramulu, Fatigue performance evaluation of selective laser melted Ti-6Al-4V, Mater. Sci. Eng. A. 598 (2014) 327–337. doi:10.1016/j.msea.2014.01.041.

[30] G. Nicoletto, G. Anzelotti, R. Konečná, X-ray computed tomography vs. metallography for pore sizing and fatigue of cast Al-alloys, Procedia Eng. 2 (2010) 547–554. doi:10.1016/j.proeng.2010.03.059.

[31] S. Siddique, M. Imran, M. Rauer, M. Kaloudis, E. Wycisk, C. Emmelmann, et al., Computed tomography for characterization of fatigue performance of selective laser melted parts, Mater. Des. 83 (2015) 661–669. doi:10.1016/j.matdes.2015.06.063.

[32] Y. Murakami, M. Endo, Effecs of defects, inclusions and inhomogeneities on fatigue strength, Fatigue. 16 (1994).

[33] H. Kitagawa, S. Takahashi, Applicability of fracture mechanics to very small cracks or cracks in the early stage, in: Proceeding Second Int. Conf. Mech. Behav. Mater., 1976: pp. 627–631.

[34] U. Zerbst, M. Vormwald, R. Pippan, H.-P. Gänser, C. Sarrazin-Baudoux, M. Madia, About the fatigue crack propagation threshold of metals as a design criterion - a review, Eng. Fract. Mech. (2016) 190–243.

[35] U. Zerbst, M. Madia, Fracture mechanics based assessment of the fatigue strength: Approach for the determination of the initial crack size, Fatigue Fract. Eng. Mater. Struct. 38 (2015) 1066–1075. doi:10.1111/ffe.12288.

[36] Y. Murakami, Metal fatigue: effects of small defects and nonmetallic inclusions, Elsevier, 2002.

[37] B. Torries, A. Imandoust, S. Beretta, S. Shao, N. Shamsaei, Overview on Microstructure- and Defect-Sensitive Fatigue Modeling of Additively Manufactured Materials, Jom. 70 (2018) 1853–1862. doi:10.1007/s11837-018-2987-9.

[38] Y. Yamashita, T. Murakami, R. Mihara, M. Okada, Y. Murakami, Defect Analysis and Fatigue Design Basis for Ni-based Superalloy 718 manufactured by Additive Manufacturing, Int. J. Fatigue. (2018). doi:10.1016/j.prostr.2017.11.054.

[39] H. Masuo, Y. Tanaka, S. Morokoshi, H. Yagura, T. Uchida, Y. Yamamoto, et al., Influence of defects, surface roughness and HIP on the fatigue strength of Ti-6Al-4V manufactured by additive manufacturing, Int. J. Fatigue. 117 (2018) 163–179. doi:10.1016/j.ijfatigue.2018.07.020.

[40] J.N. Domfang Ngnekou, Y. Nadot, G. Henaff, J. Nicolai, W.H. Kan, J.M. Cairney, et al., Fatigue properties of AlSi10Mg produced by Additive Layer Manufacturing, Int. J. Fatigue. 119 (2019) 160–172. doi:10.1016/j.ijfatigue.2018.09.029.

[41] S. Beretta, Affidabilità delle costruzioni meccaniche, Springer, Milano, 2009. doi:10.1007/978-88-470-1079-6.

[42] S. Romano, S. Miccoli, S. Beretta, A new FE post-processor for probabilistic fatigue assessment in the presence of defects and its application to AM parts, Int. J. Fatigue. 125 (2019) 324–341.

[43] S. Coles, An Introduction to Statistical Modeling of Extreme Values, Springer London, London, 2001. doi:10.1007/978-1-4471-3675-0.

[44] R.-D. Reiss, M. Thomas, Statistical Analysis of Extremes Values, third, Birkhäuser, 2007.

[45] ASTM E2283 - 08(2014), Standard Practice for Extreme Value Analysis of Nonmetallic Inclusions in Steel and Other Microstructural Features, (2014). doi:10.1520/E2283-08R14.2.

[46] ASTM E45-18a, Standard Test Methods for Determining the Inclusion Content of Steel, (2018). doi:10.1520/E0045-13.2.

[47] D.W. Hetzner, Developing ASTM E2283: Standard Practice for Extreme Value analysis of Nonmetallic Inclusions in Steel and Other Microstructural Features, J. ASTM Int. (2007) 1–28. doi:10.1520/E2283-

08R14.2.

[48] A.C. Davison, R.L. Smith, Models for Exceedances over High Thresholds, J. R. Stat. Soc. Ser. B. 52 (1990) 393–442.

[49] C.W. Anderson, G. Shi, H. V. Atkinson, C.M. Sellars, J.R. Yates, Interrelationship between statistical methods for estimating the size of the maximum inclusion in clean steels, Acta Mater. 51 (2003) 2331–2343. doi:10.1016/S1359-6454(03)00041-7.

[50] S. Romano, A.D. Brandão, J. Gumpinger, M. Gschweitl, S. Beretta, Qualification of AM parts: Extreme value statistics applied to tomographic measurements, Mater. Des. 131 (2017) 32–48. doi:10.1016/j.matdes.2017.05.091.

[51] J. Hinebaugh, M. George, C. Metcalfe, Use of MicroCT for Powder Bed Metal Additive Manufacturing Parameter Development and Machine Qualification, in: ASTM Symp. Struct. Integr. Addit. Manuf. Parts, Washington D.C., 2018.

[52] P. Wang, X. Tan, C. He, M. Ling, S. Nai, R. Huang, Scanning optical microscopy for porosity quanti fi cation of additively manufactured components, Addit. Manuf. 21 (2018) 350–358. doi:10.1016/j.addma.2018.03.019.

[53] M. Mohammadi, H. Asgari, Achieving low surface roughness AlSi10Mg_200C parts using direct metal laser sintering, Addit. Manuf. 20 (2018) 23–32. doi:10.1016/j.addma.2017.12.012.

[54] S.D. Wicksell, The Corpuscle Problem: A Mathematical Study of a Biometric Problem, Biometrika. 17 (1925) 84–99.

[55] S.D. Wicksell, The Corpuscle Problem: Second Memoir: Case of Ellipsoidal Corpuscles, Biometrika. 18 (1926) 151–172.

[56] C.W. Anderson, J. De Maré, H. Rootzén, Methods for estimating the sizes of large inclusions in clean steels, Acta Mater. 53 (2005) 2295–2304. doi:10.1016/j.actamat.2005.01.035.

[57] Y. Uemura, Y. Murakami, A Numerical Simulation of Evaluating the Maximum Size of Inclusions to Examine the Validity of the Metallographic Determination of the Maximum Size of Inclusions, Trans. Japan Soc. Mech. Eng. Ser. A. 56 (1990) 162–167.

[58] R. Takahashi, M. Sibuya, The maximum size of the planar sections of random spheres and its application to metallurgy, Ann. Inst. Stat. Math. 48 (1996) 127–144. doi:10.1007/BF00049294.

[59] E. Wycisk, C. Emmelmann, S. Siddique, F. Walther, High Cycle Fatigue (HCF) Performance of Ti-6Al-4V Alloy Processed by Selective Laser Melting, Adv. Mater. Res. 816–817 (2013) 134–139. doi:10.4028/www.scientific.net/AMR.816-817.134.

[60] Y. Murakami, S. Kodama, S. Konuma, Quantitative evaluation of effects of non-metallic inclusions on fatigue strength of high strength steels. I: Basic fatigue mechanism and evaluation of correlation between the fatigue fracture stress and the size and location of non-metallic inclusions, Int. J. Fatigue. 11 (1989) 291–298. doi:https://doi.org/10.1016/0142-1123(89)90054-6.

[61] E.J. Gumbel, Statistics of extremes, Courier Corporation, 2012.

[62] S. Beretta, Y. Murakami, Statistical Analysis of Defects for Fatigue Strength Prediction and Quality Control of Materials, Fatigue Fract. Eng. Mater. Struct. 21 (1998) 1049–1065. doi:doi:10.1046/j.1460-2695.1998.00104.x.

[63] S. Beretta, C.W. Anderson, Y. Murakami, Extreme value models for the assessment of steels containing multiple types of inclusion, Acta Mater. 54 (2006) 2277–2289. doi:10.1016/j.actamat.2006.01.016.

[64] S. Beretta, Y. Murakami, Largest-extreme-value distribution analysis of multiple inclusion types in determining steel cleanliness, Metall. Mater. Trans. B Process Metall. Mater. Process. Sci. 32 (2001) 517–523. doi:10.1007/s11663-001-0036-4.

[65] G. Shi, H. V. Atkinson, C.M. Sellars, C.W. Anderson, Application of the Generalized Pareto Distribution to the estimation of the size of the maximum inclusion in clean steels, Acta Mater. 47 (1999) 1455–1468. doi:10.1016/S1359-6454(99)00034-8.

[66] E. Maire, P.J. Withers, Quantitative X-ray tomography, Int. Mater. Rev. 59 (2013) 1–43. doi:10.1179/1743280413y.0000000023.

[67] J. Gumpinger, A.D. Brandao, E. Beevers, T. Rohr, T. Ghidini, S. Beretta, et al., Expression of Additive Manufacturing Surface Irregularities Through a flaw-Based Assessment, Accept. ASTM Sel. Tech. Pap. (2019).

[68] M. Seifi, M. Gorelik, J.M. Waller, N. Hrabe, N. Shamsaei, S. Daniewicz, et al., Progress Towards Metal Additive Manufacturing Standardization to Support Qualification and Certification, Jom. 69 (2017) 439–455. doi:10.1007/s11837-017-2265-2.

[69] A. du Plessis, P. Sperling, A. Beerlink, L. Tshabalala, S. Hoosain, N. Mathe, et al., Standard method for microCT-based additive manufacturing quality control 4: Metal powder analysis, MethodsX. 5 (2018) 1336–1345. doi:10.1016/j.mex.2018.09.006.